

# Vat photopolymerization 3D printing of yttria-stabilized ZrO<sub>2</sub> ceramics: effects of a sintering additive (Na<sub>2</sub>O – 2SiO<sub>2</sub>), biocompatibility, and osteointegration

S.V. Smirnov<sup>a,\*</sup>, P.V. Protsenko<sup>b,1</sup>, M.A. Goldberg<sup>a</sup>, T.O. Obolkina<sup>a</sup>, O.S. Antonova<sup>a</sup>, K.V. Malyutin<sup>c</sup>, G.P. Kochanov<sup>a</sup>, A.A. Konovalov<sup>a</sup>, Yu.M. Nevolin<sup>d</sup>, A.V. Volkov<sup>e</sup>, S.A. Akhmedova<sup>f</sup>, V.A. Kirsanova<sup>f</sup>, I.K. Sviridova<sup>f</sup>, N.S. Sergeeva<sup>f</sup>, S.M. Barinov<sup>a</sup>, V.M. Ievlev<sup>a</sup>, V.S. Komlev<sup>a,\*</sup>

<sup>a</sup> A.A. Baikov Institute of Metallurgy and Materials Science, Russian Academy of Sciences, 119334, Leninsky pr., 49, Moscow, Russian Federation

<sup>b</sup> M.V. Lomonosov Moscow State University, Department of Chemistry, 119991, Leninskie Gory, 1, Moscow, Russian Federation

<sup>c</sup> Non-Profit Organization Development Foundation of the Center for the Development and Commercialization of New Technologies, 121205, the territory of the innovation center "Skolkovo", Nobel st. 5, Moscow, Russian Federation

<sup>d</sup> Frumkin Institute of Physical Chemistry and Electrochemistry, Russian Academy of Sciences, 119071, Leninsky Prospekt, 31, bldg. 4, Moscow, Russian Federation

<sup>e</sup> Central Pathology Laboratory, Avtsyn Research Institute of Human Morphology of FSBSI "Petrovsky National Research Centre of Surgery", 119991, Abrikosovsky lane, 2, Moscow, Russian Federation

<sup>f</sup> P.A. Herzen Moscow Research Oncology Institute – branch of National Medical Research Radiological Centre (affiliated with Ministry of Health of Russian Federation), 125284, 2nd Botkinsky Pass. 3, Moscow, Russian Federation

## ARTICLE INFO

### Keywords:

Yttria-stabilized ZrO<sub>2</sub>  
Sintering additive  
3D printing  
Vat photopolymerization

## ABSTRACT

Effects of a liquid-phase sodium disilicate additive on the properties of ZrO<sub>2</sub> ceramics containing 3 mol.% of Y<sub>2</sub>O<sub>3</sub> and 2 wt% of Al<sub>2</sub>O<sub>3</sub> are presented, including phase composition, microstructure, shrinkage, porosity, and bending strength. The distribution of elements along grain boundaries and the composition in a selected area of a lamella were investigated by transmission electron microscopy in pure and additive-containing samples. As a result of the introduction of the additive, sintering activity of the material increased, and the sintering temperature diminished down to 1150 °C. Thus, dense nanocrystalline materials with a crystallite size of 50–70 nm and a bending strength of up to 450 MPa were obtained. Optimized polymer-ceramic suspensions were used to produce objects with complex geometric shapes by 3D molding technology through layer-by-layer vat polymerization. According to *in vitro* assays, the obtained samples are nontoxic and cytocompatible with human osteosarcoma MG-63 cells, and according to *in vivo* experiments, are biocompatible and showing osseointegrative properties when implanted into the rat tibia.

## 1. Introduction

Yttria-stabilized ZrO<sub>2</sub> (YSZ) is a widely used ceramic with a unique combination of functional properties including high strength, chemical and thermal stability, biocompatibility, and the absence of cytotoxicity [1]. Many factors including crystallite size, phase composition, and microstructure influence the strength of YSZ. A decrease in the sintering temperature makes it possible to obtain ceramics with smaller grain size by retarding recrystallization. This approach also requires a smaller

amount of a stabilizer to prevent the tetragonal-monoclinic transition of YSZ through cooling [2,3]. All this leads to higher strength of the final structure [4,5]. With a decrease in the sintering temperature of ceramics down to 1200 °C, it becomes possible to use less expensive furnace equipment and to avoid hot or isostatic pressing. Recently, advantages of 3D printing stereolithography methods (SLA) and digital light processing (DLP) for the production of ceramic parts of complex shape and structure were demonstrated. The technology requires concentrated ceramic/polymer slurries (30–60 vol%) [6]. DLP technology involves a

\* Corresponding authors.

E-mail addresses: [ssmirnov@imet.ac.ru](mailto:ssmirnov@imet.ac.ru) (S.V. Smirnov), [komlev@mail.ru](mailto:komlev@mail.ru) (V.S. Komlev).

<sup>1</sup> Both researchers are senior authors in this paper.

<https://doi.org/10.1016/j.addma.2024.104071>

Received 20 November 2023; Received in revised form 16 February 2024; Accepted 7 March 2024

Available online 8 March 2024

2214-8604/© 2024 Elsevier B.V. All rights reserved.

liquid photopolymer resin, which is polymerized layer by layer under the action of a light screen with a certain wavelength suitable for the photoinitiator [7]. This method allows to obtain printed models of complex shapes with high accuracy (down to 10 microns) and preset internal structure. One could produce individual implants in accordance with a patient's computer tomography data for personalized approach [8–11]. This could be also applied to the production of ram-navicular, calcaneal-cuboid, and knee joints. Nonetheless, the process of printing 3D ceramic structures has considerable limitations due to the difficulty of obtaining blanks with intimate contact between powder particles. This drawback leads to the formation of defects (cracks, deformations, and disintegration) during the removal of the binder polymer (debinding) and during the sintering of ceramics. Washing of a green body in PEG-400 and prolonged low-temperature pyrolysis including a vacuum stage has been proposed for DLP-printed 5.35 wt%  $Y_2O_3$ - $ZrO_2$  [12] and  $Al_2O_3$  [13] for solving the problems with cracking. Another issue is the deformation of printed models during the burning of the binding organic matter. In ref. [14], a preventive effect of ultradispersed sintering-active powders against cracking and deformation during pyrolysis was demonstrated. The application of the highly active ceramic powder as well as sintering additives could be employed for decreasing the sintering temperature, for enhancing green-body strength, and for preventing cracking during the debinding. It has been shown that the addition of  $SiO_2$  leads to an increase in the zirconia sintering rate owing to liquid-phase formation [15]. Similar results have been obtained for  $Al_2O_3$ - $ZrO_2$  ceramics containing sodium silicate in the course of microwave hybrid heating [16]. Recently, we demonstrated a decrease in the sintering temperature for  $ZrO_2$ - $Al_2O_3$  composite materials owing to the formation of low-temperature melts based on sodium silicates and transitional metal oxides; for partially stabilized  $ZrO_2$  nanopowders, the sintering temperature was reduced by more than 350 °C because of the introduction of sodium disilicate as a liquid-phase additive [17,18]. The use of an  $Al_2O_3$  additive allows to improve mechanical properties of partially stabilized  $ZrO_2$  without raising the sintering temperature [19]. Recently, an  $Al_2O_3$ - $ZrO_2$  ceramic composite was successfully used for 3D printing by the SLA method; optimization of slurry viscosity and sintering temperature contributed to the formation of  $Al_2O_3$ - $ZrO_2$  ceramic materials with high microhardness and fracture toughness [20]. At the same time, the large surface area of such powders results in a decrease of the sintering temperature. For example,  $ZrO_2$  nanopowders with a surface area of 160 m<sup>2</sup>/g are characterized by crystallization and low-temperature pre-sintering starting from 400 °C [21]. Thus, such effects could help to strengthen a green body at the stage of pyrolysis.

This work was aimed at finding the composition of the slurry suitable for DLP 3D printing and at developing technological modes of debinding and sintering of  $ZrO_2$  high-precision ceramic parts. We lowered the sintering temperature of  $ZrO_2$  ceramics thanks to the application of active nanopowders and introduction of a sintering additive based on the  $Na_2O$ - $2SiO_2$  system and prevented the cracking and deformation of the ceramic printed parts. Currently, there is limited literature on additives for zirconium dioxide that form a liquid phase within the temperature range specified. The liquid stage temperatures for  $Na_2SiO_3$  and  $Na_2Si_2O_5$  are 1070 °C and 863 °C, respectively [22]. We have revealed high efficiency in sintering temperature reduction of the additive  $Na_2SiO_3$  which is monosilicate [23,24]. To achieve our goal in 3D printing, we introduced additives with lower melting points, such as  $Na_2Si_2O_5$ , which has a melting point of 863 °C and also forms a eutectic in the  $ZrO_2$ - $Na_2SiO_3$  system [25]. The material's mechanical and biological properties were investigated, and good potential of the obtained ceramics for biomedical applications was demonstrated.

## 2. Experimental part

### 2.1. Synthesis of powder material

To obtain 100 g of powder of  $ZrO_2$  containing 3 mol.% of  $Y_2O_3$

(3YSZ) doped with 2 wt% of  $Al_2O_3$ , chemical coprecipitation at room temperature was performed. All salts were of analytical grade, supplied by Labtech. A mixture of  $ZrOCl_2 \cdot 8H_2O$  (242.4 g),  $YCl_3 \cdot 6H_2O$  (14.1 g) (corresponding to the following composition: 97 mol.% of  $ZrO_2$  and 3 mol.% of  $Y_2O_3$ ), and  $AlCl_3 \cdot 6H_2O$  (9.6 g) dissolved in 450 mL of distilled  $H_2O$  was added dropwise with stirring to a precipitating solution. The precipitating solution was prepared by the dilution of 200 mL of 25%  $NH_4OH$  with 370 mL of distilled water with the subsequent dissolution of 125 g of  $NH_4HCO_3$  in it. Stirring was continued for 1 h after the addition was finished. The resulting gel was dried for 3 days at 80 °C and heated at 650 °C for 3 h in ambient air, ground up in a planetary ball mill using  $ZrO_2$  grinding bodies for 30 min in ethanol as the medium, air-dried, and mechanically rubbed through a nylon sieve with a mesh size of 60 μm.

The resultant powder material was named 3YSZ-1. To obtain a ceramic with a  $Na_2Si_2O_5$  liquid-phase sintering additive, the precipitating solution was modified by the addition of 8 mL tetraethoxysilane before the dropwise addition to the mixture of chloride salts. The precipitated powders were treated similarly to 3YSZ-1. Additionally, the obtained powder was mixed with a 11%  $Na_2SiO_3$  aqueous solution. The amount of introduced  $Na_2SiO_3$  corresponded to 5 wt% of  $Na_2Si_2O_5$  in the final powders. This material was named 3YSZ-2.

### 2.2. Characterization of the powders

Specific surface area of the obtained powders was measured using a Tristar 3000 Micromeritics device (USA) by the BET nitrogen adsorption method. Morphology of the powders was investigated by transmission electron microscopy (TEM) (JEM 2100, JEOL, Japan, carbon-sputtered specimens). The parameters of lattice and phase composition were determined by the electron diffraction (ED) obtained by TEM. The identification of the electron diffractograms was performed with CrysTBox software [26]. X-ray phase analysis (XRD) was performed on Difrax 401 (JSC Scientific Instruments, Russia)  $\lambda CrK\alpha$  (2.29100 Å) diffractometer with  $2\theta$  from 10° to 80° with a step of 0.01°.

### 2.3. Preparation of ceramics through pressing and sintering

Powders 3YSZ-1 and 3YSZ-2 were shaped in steel molds without any plasticizers by uniaxial pressing at 200 MPa to produce  $3 \times 3 \times 30$  mm bars. The samples were sintered in air in the temperature range of 1100–1450 °C (Fig. 6C) for 2 h and additionally at 1250 °C for 5 h. Microstructure, phase composition, and mechanical properties of the obtained samples were investigated next. For the dilatometric analysis, the cylinders with the diameter and height of 3 and 7.2 mm, respectively, were created by pressing similarly. For *in vitro* assays, ceramic granules were obtained by uniaxial pressing at 200 MPa, sintering at 1450 °C, grinding in an agate mortar, and sorting on a nylon sieve to obtain the fraction of 300–800 μm.

### 2.4. Ceramic fabrication by DLP 3D printing

For the formation of samples by DLP 3D printing, a suspension was prepared in the following way: powder 3YSZ-1 or 3YSZ-2 was mixed with a photoactive resin based either on a liquid oligomer-containing benzophenone-type photoinitiator designated as Metacryl-1 (M1) or on purchased AnyCubic Basic Clear (AC) (from a commercial source) in a mass ratio of 1:1 by means of overhead stirrer IKA R1, followed by ultrasonication with a Bandelin Sonopuls HD 2070/2200 disperser (Germany). The printing was performed by means of DLP 3D printer AnyCubic photon S (China) with colorful LCD, the light source diodes emit at a luminous intensity of 280000 lx, a wavelength of 405 nm and a power of 84 W, printing parameters: layer thickness of 35 μm at room temperature with an exposition of 180 s [27]. The printed samples were constructed in accordance with STL files models built in Autodesk Fusion (USA) software in the form of bars with the size of  $3 \times 3 \times 30$  mm

and mesh structure with a mesh step of 1.5 mm. The following models were printed: bone structure (thing: 3750517), a model of a fragment of a DNA molecule (thing: 1810631), a gyroid with a wall thickness of 200 microns (thing: 757884, from the open database <https://www.thingiverse.com>; other sources: a model of an earphone case with a complex shape). After the printing, the samples were washed in ethanol to remove the uncured resin. The samples were processed by low-temperature pyrolysis (debinding) [28] of the organic binder in nitrogen in the temperature range 25–360 °C for 120 h (Fig. 6B). The resulting green bodies were sintered at 1500 and 1600 °C in air for 2 h.

## 2.5. Characterization of the materials

Granulometric composition of the powders was assessed by laser particle analyzer FRITTSCH Analysette 22 (Fritsch, Idar-Oberstein, Germany). Dilatometric analyses of the compressed cylinders were carried out on a DIL 402 C dilatometer (Netzsch, Germany) with a vacuum-tight furnace in an argon atmosphere (purity 99.999%) in the temperature range 25–1400 °C at a heating rate of 10 °C/min followed by isothermal exposure for 5 h at 1400 °C. XRD characterization of the compressed and printed bars after sintering was performed on Difrax 401. Each material's microstructure was investigated by scanning electron microscopy (SEM) by means of Tescan Vega II (Czech). To reveal internal microstructure of the compressed samples, the ceramic bars were polished, thermally etched at a temperature 100 °C lower than the initial sintering temperature for 1 h [29], and gold-coated by magnetron sputtering on a Q150R ES Quorum Technologies device (UK). The survey was carried out at an accelerating voltage of 20 kV using a secondary electron (SE) and backscattered electron (BSE) detector. Samples for TEM were prepared from the compressed and sintered bars on a Helios DualBeam NanoLab 600i (FEI) device using a Ga<sup>+</sup> focused ion beam (FIB). Sections were prepared according to the following algorithm: 1) a protective layer (~1.5 × 3 × 16 μm) made of carbon and platinum was formed on the samples' surface by a gas-engineering system (GES); 2) on both sides of the protective layer using the FIB over an area of ~8 × 16 μm, the sample material was sprayed to a depth of ~4 μm; 3) the created lamella was cut along the perimeter using the FIB, and the lamella was removed; 4) using GES, a lamella was attached to a copper electron microscopic grid (microscopic sample holder). Shooting mode, a scanning transmission electron microscope (STEM) with a field emission electron gun AEP (field emission gun FEG STEM) using dark-field (HAADF) and bright-field (BF) detectors on TITAN 80–300 (USA) were employed for microscopy including the z-contrast method. Open porosity was measured by the hydrostatic weighing method based on the Archimedes force determination according to GOST 10180-78 (official quality standard in Russia). Mechanical tests of the sintered bars were performed by the three-point bending method on Instron 5800 ASTM C1161 (USA); five samples per point were analyzed. The viscosity of the suspension and of photoactive resin was determined using a Rheotest RV 2.1 rotational viscometer (VEB MLW Prüfgeräte-Werk Medingen, DDR) (rotation speed 0.28–243 rpm, torque 0.1–98.1 mNm). Film thickness of the different slurries was measured using optical microscope Biolam LOMO (USSR). To obtain each sample of the polymerized film, 2 mL Eppendorfs were used in the vat of AnyCubic Photon S 3D printer. Sedimentation stability was determined by visual inspection of the initially homogenized suspension in transparent test tubes. Differential thermal analysis/thermogravimetry (DTA/TG) curves were recorded using a Netzsch STA Jupiter 449 F3 (Germany) thermoanalytical complex in the range of 25–1000 °C; the samples were heated in 300 μL corundum crucibles in both nitrogen atmosphere (purity 99.999%) and air at a heating rate of 10 °C/min. To obtain an air atmosphere for the investigation, streams of N<sub>2</sub> and O<sub>2</sub> were mixed in a ratio of 8:2. Digital photographs in the macro mode were taken with a 5 MP OmniVision Camera (China) OV5675 1/5" sensor behind a telemacro f/2.4 lens.

## 2.6. In vitro assays of cytocompatibility

The evaluation of the cytocompatibility of 3YSZ-1 and 3YSZ-2 ceramic samples was carried out on the human osteosarcoma MG-63 cell line (Russian Collection of Cell Cultures, Institute of Cytology RAS, St. Petersburg, Russia) via direct contact of the test culture with the surface of the test samples. Sterile (180 °C, 2 h, Binder, Germany) materials were placed into wells of 96-well culture plates (Costar, USA), in quadruplicate for each investigated time period, including one well for the control: optical blank. The cell suspension was added at a concentration of 20.0 × 10<sup>3</sup>/well (seeding density: 60.0 × 10<sup>3</sup> cells/cm<sup>2</sup>) in 200 μL of a complete growth medium (CGM) having the following composition: the DMEM medium (PanEco, Russia), 10% of fetal calf serum (HyClone, USA), 4 mM glutamine, a 1 M HEPES solution (PanEco, Russia), and a gentamicin solution (final concentration 50 μg/mL, Dalchimpharm, Russia). Wells with the cells (in the CGM) on polystyrene culture plastic (instead of the ceramics) served as a control.

Cultivation was performed in a CO<sub>2</sub> incubator (Sanyo, Japan) at 37 °C and 5% of CO<sub>2</sub> for 1, 4, and 6 days with twice-a-week refreshment of the medium. All manipulations with materials and cells were carried out in a sterile box in a class II laminar flow cabinet (Heraeus, Germany).

The viability of MG-63 cells was determined by the MTT assay [30] and the Live/Dead kit. The first method is based on the ability of dehydrogenases in live cells to reduce 3-(4,5-dimethylthiazolyl-2)-5-diphenyltetrazolium bromide (MTT, Sigma, USA) to water-insoluble blue formazan crystals. As shown earlier, the amount of formed formazan can characterize not only the metabolic but also the proliferative activity (viability/cell number) of various types of human and animal cells. To conduct the MTT assay, at the end of cultivation, 50 μL of the CGM was taken from each well and 25 μL of the MTT solution at a concentration of 5 mg/mL was added. After 3 h of incubation (5% CO<sub>2</sub>, 37 °C), the entire medium was decanted from each well. The resulting formazan was dissolved in isopropyl alcohol (200 μL per well, Chemmed, Russia). The precipitate that formed because of precipitation of proteins in isopropanol was removed by centrifugation of the plates for 10 min at 3000 rpm (B4i, Jouan, France). Next, 100 μL of the supernatant was transferred from each well to a 96-well flat-bottom plate (Costar, United States), and optical density of the formazan solution was evaluated on a Multiscan FC spectrophotometer (Thermo Scientific, United States) at a wavelength of 540 nm.

For 3YSZ-1 and 3YSZ-2 samples, the population of viable cells (PVC) was calculated in the experiment in relation to the control (in%) using the formula:

$$PVC = (OD_{\text{exp}}/OD_{\text{control}}) \times 100\%,$$

where OD<sub>exp</sub> and OD<sub>control</sub> are the optical density of the formazan solution in the experiment and in the control, respectively. A ceramic sample was considered cytocompatible at a PVC of ≥70%.

During the experiment, the proliferation of MG-63 cells on the surface of the samples of zirconium-containing ceramics (Olympus stereo magnifier, Japan) was monitored visually.

The data were processed by standard methods of variance statistics using the Microsoft Excel 2000 software package. The significance of differences was assessed by Student's parametric *t* test. Differences were considered statistically significant at *p* < 0.05.

## 2.7. In vivo experiments

The principles of laboratory animal care and use as well as national laws were followed. All procedures were approved by decision #2-SI-00009 (of 4 August 2021) of the Commission on Bioethical Control over the Maintenance and Use of Laboratory Animals for Scientific Purposes of the National Medical Research Radiological Centre affiliated with the Ministry of Health of the Russian Federation.

### 2.7.1. Osteointegration assessment

Osseointegrative properties of ceramic samples were studied in a

model of a bone defect (perforation defect of the tibia) in male rats. Twenty 12-week-old male Wistar rats with a body weight of 180–200 g were randomized into an implantation group and a negative-control group without implantation (the bone defect under a blood clot). Before the surgical procedure, the rats were anesthetized with Zoletil 100 (35 µg/g body weight) and Xylazine (7.5 µg/g body weight) by intramuscular injections. Next, with the animal lying on its back, a 2.0–2.5 cm skin incision was made along the inner medial surface of the tibia. The bone was cleansed of the periosteum (to exclude physiological regeneration of bone tissue). Then, on the border of the upper third of the bone using a bur with a hard-alloy cutter having a low-abrasive surface (TVS 21231; Kristall LLC, Russia), a monocortical perforation defect was created, penetrating into the bone canal and coinciding with the size of the cone-shaped 3D construct, produced by DLP technologies developed in this paper. The defect was filled by the sterilized (180 °C, 2 h, Binder, Germany) 3D construct. In the negative-control group, the bone defects created similarly were left empty and healed under blood clots. At the final stage of the operation, layer-by-layer sutures were applied to the muscles and skin of the tibia (Fig. 8C). After the surgical procedure, all animals received a single dose of anti-inflammatory drug Tolfedine, 4.0 mg/kg (Vetoquinol, France), and Levomekol ointment was applied to the wound (NizhFarm, Russia). The rats were returned to their cages and housed with free access to water and feed. At 4 weeks after implantation, the rats were euthanized in a CO<sub>2</sub> chamber (TEC-NIPLAST; Italy), and the operated tibia were excised for histopathological analysis.

### 2.7.2. Histopathological analysis

The samples were subdivided into two groups. The first one was examined after the samples' extraction from an animal. The 3D constructs were extracted with minimal damage to the adjacent bone. The biological materials were decalcified in an EDTA solution (0.3 M, 37 °C, 25–30 days) and then embedded in paraffin. Tissue Section (5 µm) were cut off on the microtome and processed for hematoxylin and eosin (H&E) staining.

The second group of the excised tibia samples was washed under tap water for 4 h with subsequent dehydration with isopropanol (Biovitrum, Russia) at increased concentration. The samples were prepared by embedding into polymer resin Technovit 900. Tissue sections (100 µm) were made by means of a BUEHLER ISOMET 4000 precision machine (Germany). The obtained sections were placed on a glass slide and polished with a BUEHLER ALPHA&BETA/VECTOR machine to decrease their thickness down to 10–15 µm using grinding wheels of descending grit (from 300 to 1200 Gr). The resulting sections were stained by the triple staining method—celestial trichrome [31]—and were examined under an Axio Lab.A1 light microscope (Zeiss, Germany) equipped with a digital camera.

Morphometric analysis was carried out in the Megamorph12 software, the relative area of contact between the implant and bone tissue, fibrous tissue, or bone marrow was determined in accordance with ref. [31].

## 3. Results

### 3.1. Powders

According to XRD results, the pure ZrO<sub>2</sub> (3YSZ-1) and additive-containing (3YSZ-2) powders had quasi-amorphous structure with a broad peak at 30.38°, 35.14°, and 49.48°, which could be attributed to tetragonal (t-ZrO<sub>2</sub>) phases (Fig. 1Bb). TEM revealed the formation of rounded particles with a size of 10–20 nm (Fig. 1Aa, 1Ab). To clarify phase composition of 3YSZ-1, the ED pattern was analyzed next (Fig. 1Ba). This pattern was obtained in the analysis of polycrystalline nanoparticles. Reflections of crystallographic planes 011, 002, 112, 121, 013, 004, 014, 032 and 034 were identified, and the formation of t-ZrO<sub>2</sub> was confirmed. According to the BET nitrogen adsorption method, the

specific surface area of 3YSZ-1 was 52 m<sup>2</sup>/g, and for 3YSZ-2, it was 42 m<sup>2</sup>/g. Table 1

The insignificant difference in particle size between 3YSZ-1 and 3YSZ-2 (D50 of 4.12 µm and 5.39 µm, respectively) (Fig. 1Ca, 1Cb). We assume that the additional operation of the additive introduction through an aqueous solution with the further evaporation resulted in the particles additional aggregation. It is evident that the absence of the ball milling led to the preservation of the agglomerates, which were significant larger - up to 14.40 µm (Fig. 1 Cc).

### 3.2. The sintering of the ceramics

The dilatometric analyses revealed an effect of the Na<sub>2</sub>Si<sub>2</sub>O<sub>5</sub> additive on the sintering of the ceramic materials (Fig. 2A). After the thermal expansion of both ceramics, the 3YSZ-1 material began to shrink at 940 °C, whereas 3YSZ-2 started to shrink at temperatures as low as 720 °C.

In the case of the 3YSZ-1 material, approximately half of the linear shrinkage occurred during the heating up to 1400 °C, whereas the other half of the shrinkage was observed during the isothermal holding at 1400 °C for 5 h. The curve showed a tendency for further continuous shrinkage. On the other hand, the 3YSZ-2 ceramic almost completely sintered during the heating, and during the isothermal holding, an insignificant decrease of samples' sizes was noted. Thus, during the isothermal holding at 1400 °C, samples 3YSZ-1 and 3YSZ-2 manifested shrinkage of 4–11% and 22–24%, respectively. For both compositions, two-stage sintering was observed with an insignificant decline of the sintering rate at the intermediate step. The highest sintering rates for 3YSZ-1 and 3YSZ-2 were observed at 1200 and 1400 °C and at 900 and 1140 °C, respectively.

The XRD analysis was performed on the compressed samples sintered in the range of 1100–1450 °C. At 1100 °C, t-ZrO<sub>2</sub> and a tiny amount of a monoclinic phase formed in 3YSZ-1. The further increase of the experiment temperature resulted in the formation of only t-ZrO<sub>2</sub> (Fig. 2Ba). The 3YSZ-2 material showed a higher degree of crystallization at 1100 °C (as compared to 3YSZ-1) and the absence of the monoclinic phase in the whole temperature range (Fig. 2Bb).

Fig. 3A presents a comparison of the pure (Aa, Ad) and additive-containing (Ab, Ae) samples after the sintering at 1250 °C in modes SE and BSE. The microstructure of 3YSZ-1 is characterized by the formation of two phases: a matrix of ZrO<sub>2</sub> (light grains, Fig. 3Ad) and Al<sub>2</sub>O<sub>3</sub> agglomerates from less than 1–5–6 µm (dark grains, Fig. 3Ae) distributed in a disorderly manner. For both phases, a fine uniform size distribution of grains was observed, and crystallite size was ~100 nm. In the case of 3YSZ-2, a uniform distribution of Al<sub>2</sub>O<sub>3</sub> areas less than 300 nm in size was observed in the ZrO<sub>2</sub> matrix. For both phases, grains with a size of ~50–70 nm were observed, which was smaller than that of the pure sample. Besides, on the surface of the polished 3YSZ-2 sample, drop-like grains with a size of ~200–400 nm formed, which could be explained by the displacement of the liquid-phase additive (Na<sub>2</sub>Si<sub>2</sub>O<sub>5</sub>) onto the surface as a consequence of the thermal etching. For 3YSZ-1, the increase in temperature up to 1450 °C led to the growth of the grain up to 100–200 nm for ZrO<sub>2</sub> and up to 200–400 nm for Al<sub>2</sub>O<sub>3</sub> and an agglomerate reduction to 2 µm (Fig. 3Ac, 3Af).

The TEM data (Fig. 3C) confirmed the grain size distribution determined by SEM. The 3YSZ-1 ceramic sintered at 1400 °C consisted of round-shape particles of 100–300 nm without noticeable porosity. The microstructure of 3YSZ-2 samples is dense and characterized by 50–300 nm grains embedded in the sodium disilicate additive. The analysis of distribution of elements in 3YSZ-1 revealed the formation of ZrO<sub>2</sub> predominately (Fig. 4a) and 3YSZ-2 (Fig. 4b) [32,33]. The spectra of 3YSZ-2 indicated a nonuniform distribution of the silicon. The enrichment with silicon correlated with depletion of zirconium, indicating localization of the silicate phase at the grains' boundaries. high-resolution TEM pictures and selected area electron diffraction SAED) spectra confirmed the XRD data. Cell planes 002, 020, 011, 110, 112, 013, and 132 the corresponding interplanar distances refer to the

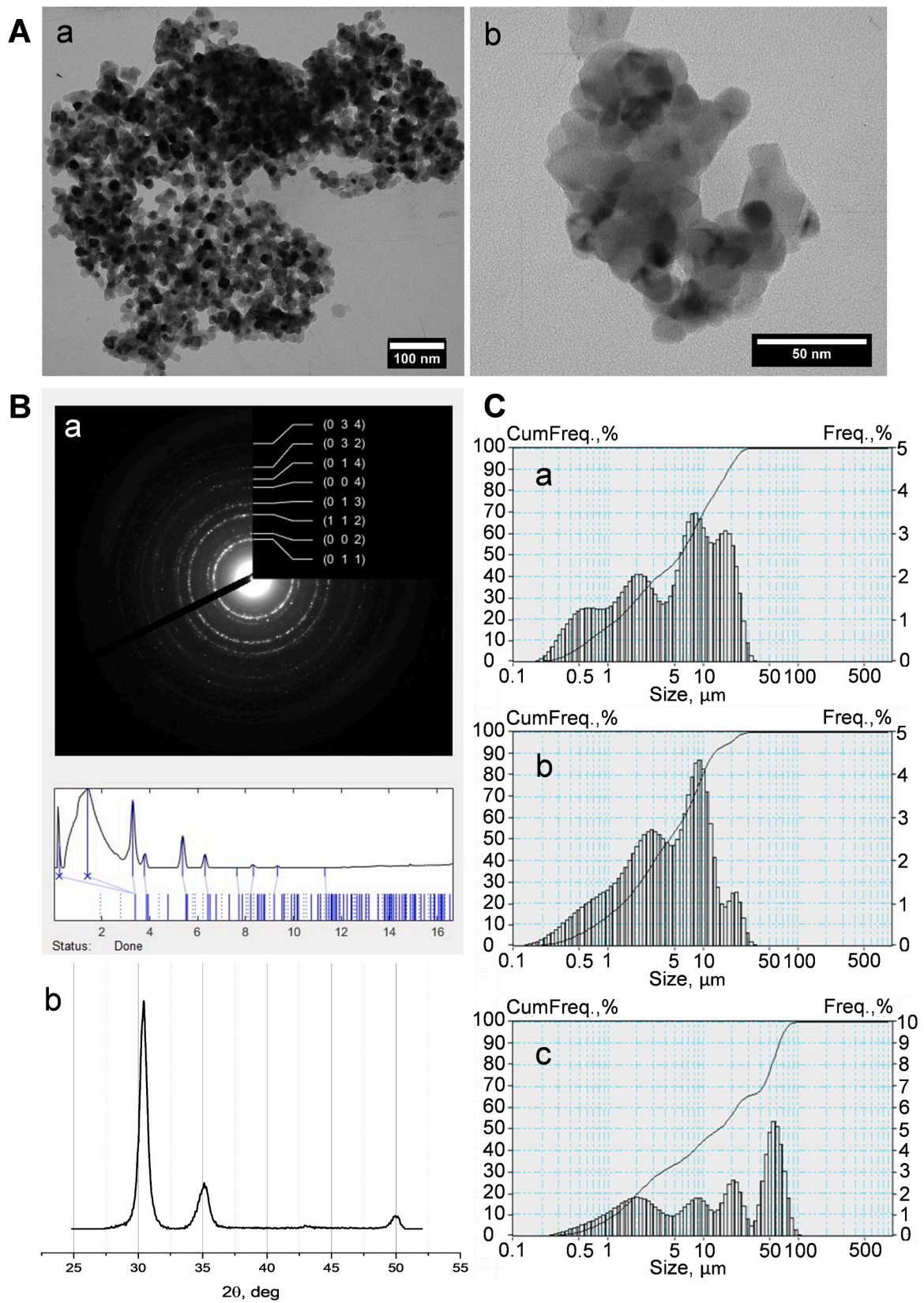


**Fig. 1.** A: TEM images of the synthesized powders 3YSZ-1 (a, b). B: Electron diffraction data (a), XRD patterns of the synthesized powders, formed by t-ZrO<sub>2</sub> (b). C: Powder particle size distribution: 3YSZ-1 after planetary ball mill (a), 3YSZ-2 after planetary ball mill (b), 3YSZ-1 without planetary ball mill (c).

**Table 1**  
The distribution properties of the powders.

Powder	D10, $\mu\text{m}$	D50, $\mu\text{m}$	D90, $\mu\text{m}$
a. 3YSZ-1	0.69	4.12	12.50
b. 3YSZ-2	0.60	5.39	17.87
c. 3YSZ-1 (no ball milling)	1.12	14.40	60.60

tetragonal p42/nmc modification of  $\text{ZrO}_2$  (Fig. 3B). For the 3YSZ-2 sample, the thin amorphous layer on the grain boundary could be attributed to the sodium disilicate additive.

Material 3YSZ-1 was sintered to a dense state at  $1350\text{ }^\circ\text{C}$  with an isothermal exposure of 2 h. The porosity did not exceed 0.5%. The bending strength of 3YSZ-1 samples was  $681 \pm 50\text{ MPa}$  after the sintering at  $1350\text{ }^\circ\text{C}$  for 2 h. The 3YSZ-2 ceramic sintered already at  $1150\text{ }^\circ\text{C}$  with 0.5% of open porosity achieved (Fig. 3D). A bending strength of 450 MPa was attained at  $1200\text{ }^\circ\text{C}$ . Extension of the holding time up to 5 h resulted in the densification of 3YSZ-1 with 677 MPa reached at  $1250\text{ }^\circ\text{C}$ ; there was no noticeable influence on 3YSZ-2.

### 3.3. Suspension properties

The rheology of the 3YSZ-1 powder (M1 suspension) was investigated in the range from 0 to 55 wt%. In the tested deformation rate range, a linear dependence of shear stress on the deformation rate was observed (Fig. 5B). This is an indication of Newtonian behavior of the studied suspensions. Shear stress values at zero shear rate are close to zero hence Bingham behavior was not observed in our systems. The viscosity of the suspensions was calculated from the stress-deformation rate dependences. An increase in the powder load caused significant growth of suspension viscosity, as presented in Fig. 5A and Table 2.

The additive influence on the thickness of the formed film depends on polymer photosensitivity and solid load components. As the  $\text{Na}_2\text{Si}_2\text{O}_5$  formed transparent film on the surface of the particles, it led to the growth of the thickness of the polymerized layer on the all exposure time range (Fig. 5C).

Sedimentation stability of 3YSZ-1 (M1 suspensions) was estimated depending on the powder load based on the time required for separation. Test tubes filled with the suspensions are presented in Fig. 5D. The 55 wt% suspension showed stability after 24 h of the experiment.

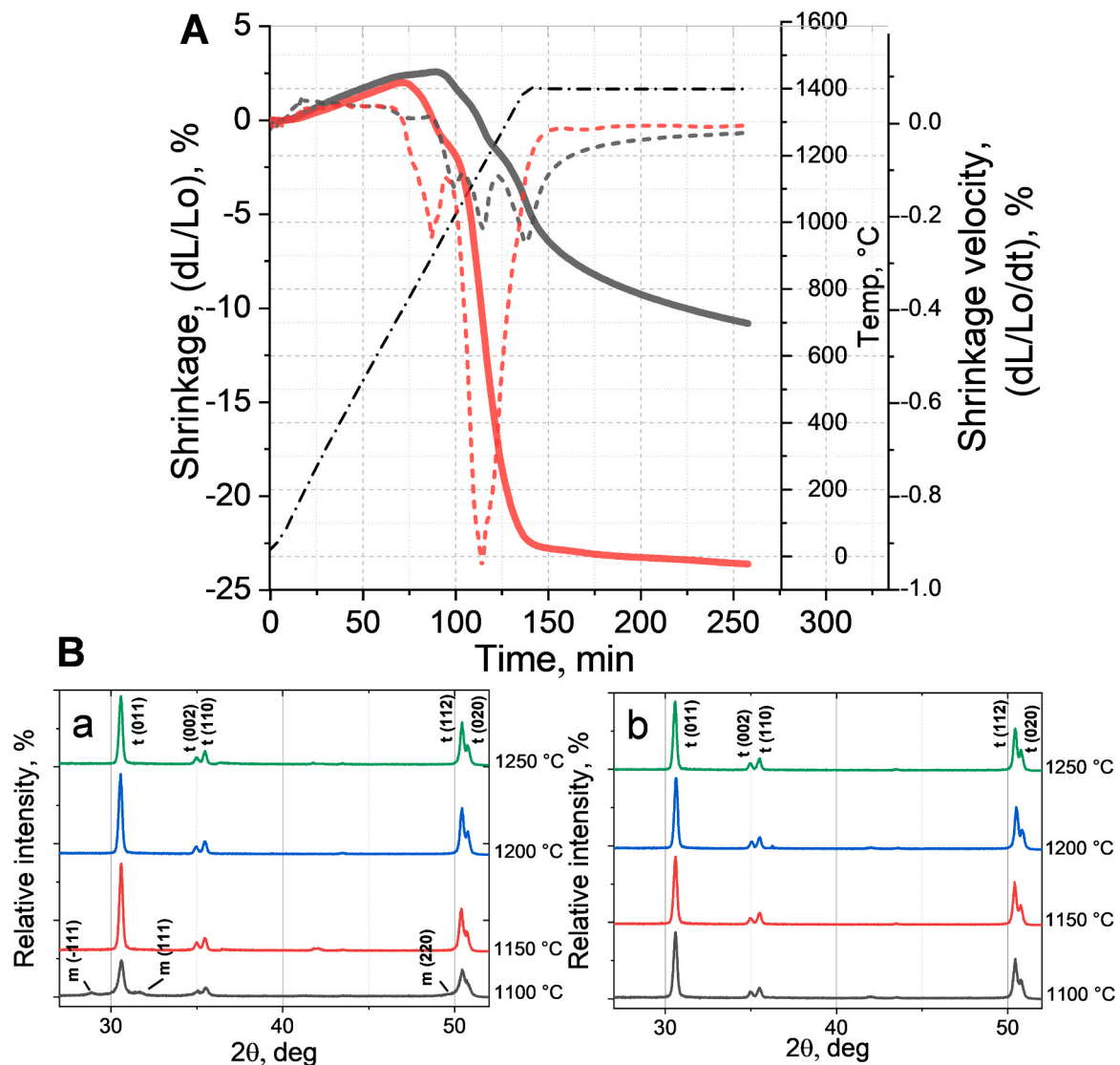


**Fig. 2.** A: Dilatometry of ceramic materials of 3YSZ-1 (solid grey line - shrinkage, dashed grey line - shrinkage rate) and 3YSZ-2 (solid red line - shrinkage, dashed red line - shrinkage rate) up to  $1400\text{ }^\circ\text{C}$  with a holding time of 2 h. B: XRD patterns of sintered samples 3YSZ-1 (a), 3YSZ-2 (b) in the temperature range of  $1100\text{--}1250\text{ }^\circ\text{C}$  with an exposure time of 2 h, where m: m- $\text{ZrO}_2$ , and t: t- $\text{ZrO}_2$ .

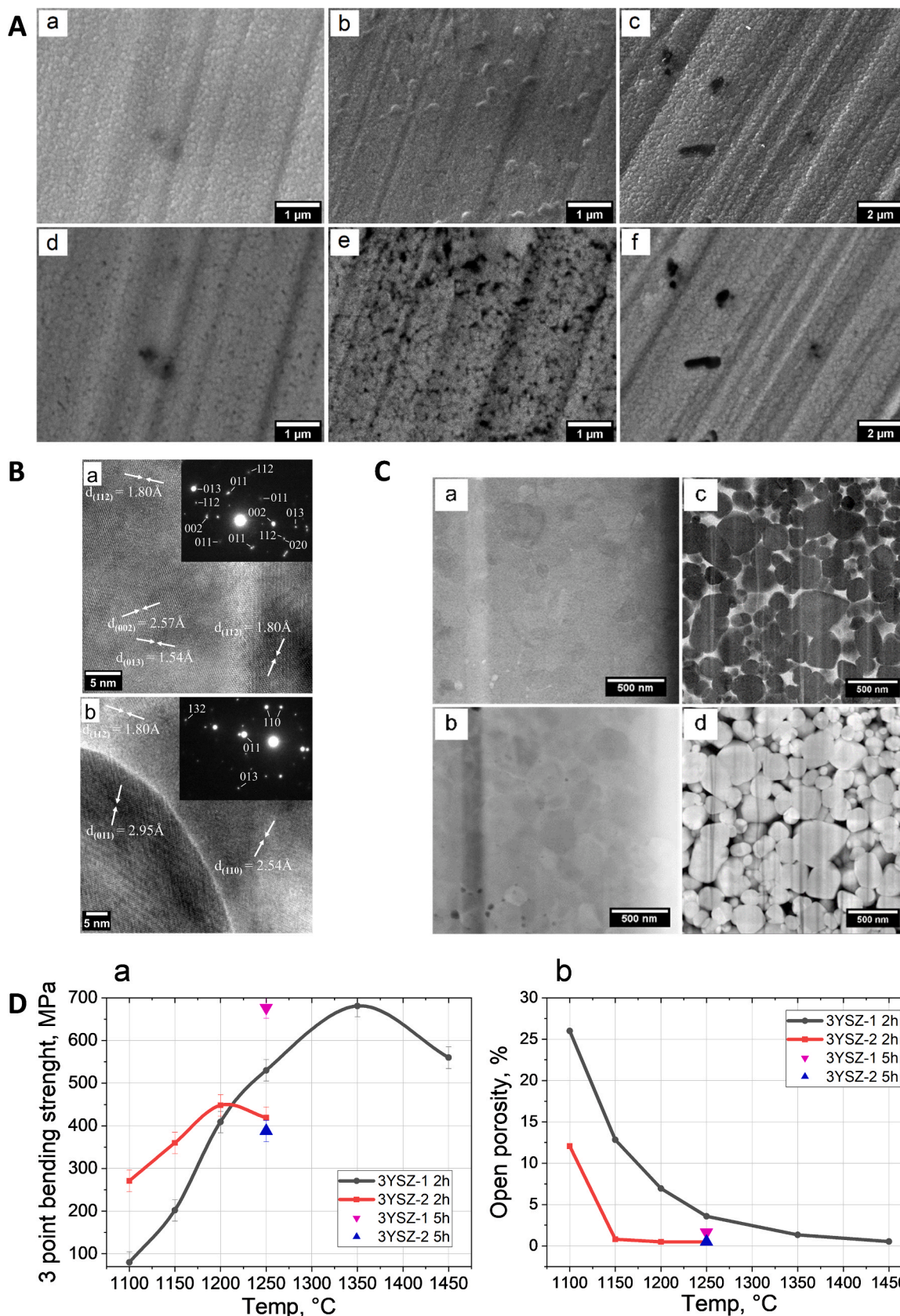


Fig. 3. A: Microstructure of sintered samples from SEM in secondary electron mode, where a - 3YSZ-1 1250 °C 2 h, b - 3YSZ-2 1250 °C 2 h, c - 3YSZ-1 1450 °C 2 h and backscattered electron, where d - 3YSZ-1 1250 °C 2 h, e - 3YSZ-2 1250 °C 2 h, and f - 3YSZ-1 1450 °C 2 h. B: TEM images and corresponding electron diffraction patterns for materials 3YSZ-1 (a) and 3YSZ-2 (b). C: TEM in z-contrast mode. Images of the ceramics structure in the bright field mode for 3YSZ-1 (a) and 3YSZ-2 (c) and in dark field mode for 3YSZ-1 (b) and for 3YSZ-2 (d). D: Flexural strength (a) and open porosity (b) as a function of sintering temperature.

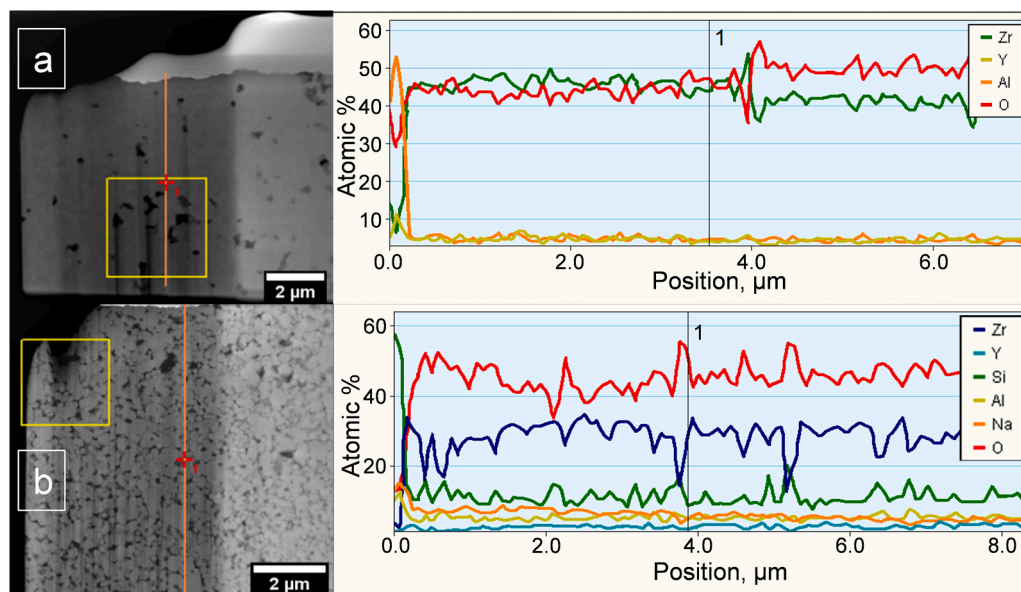


Fig. 4. Distribution of elements on the lamellar section from TEM data. The selected areas of materials 3YSZ-1 (a) and 3YSZ-2 (b), and the distribution of elements in atomic percentages for these zones.

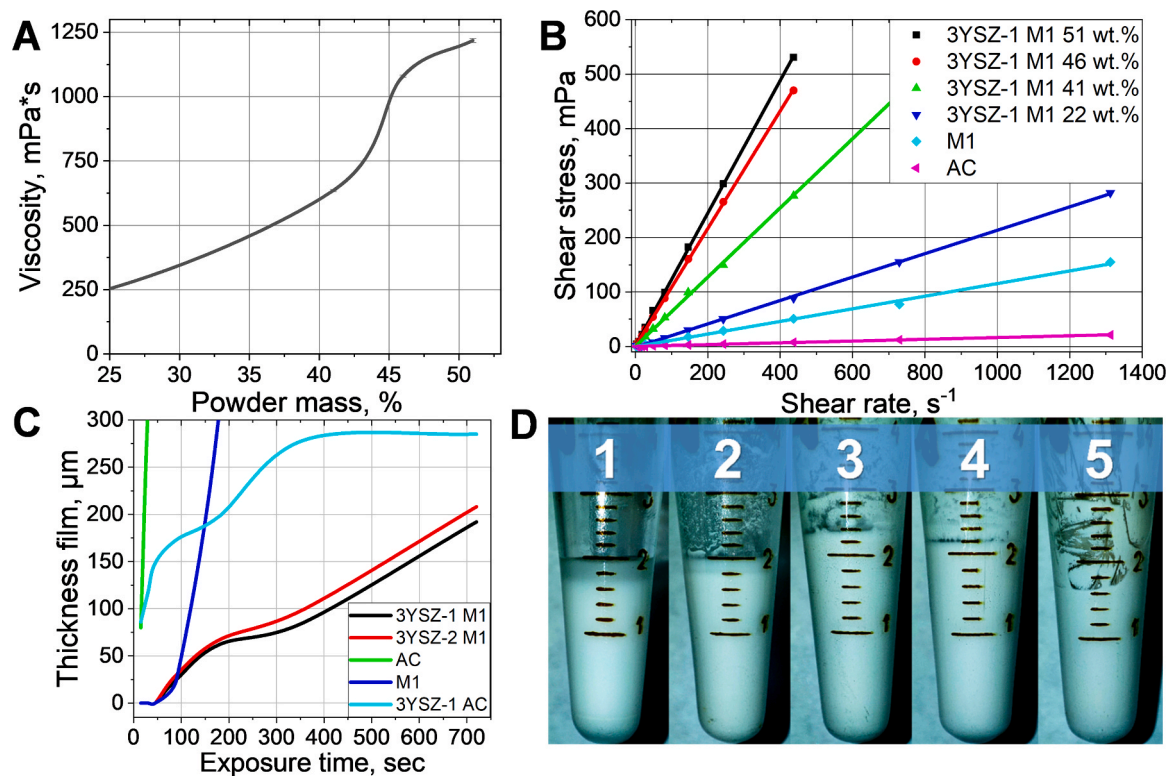


Fig. 5. A: Changes in the dynamic viscosity of the suspension with M1 as a function of the amount of filler  $ZrO_2$  powder. B: Shear thinning characteristics for different suspension load and pure polymers. C: Curing thickness of the slurries. D: Sedimentation stability of suspensions containing different amount of 3YSZ-1 powder. 1: 10 wt%, 2: 30 wt%, 3: 50 wt%, 4: 55 wt%, 5: 67 wt%.

### 3.4. 3D printing

The suspensions of 3YSZ-1 and 3YSZ-2 in M1 with a solid content of 20–55% of the photopolymer were prepared and printed by DLP technology. Optimal quality of the 3D printing was observed with the suspension containing 55 wt% of the solid phase. Samples in the form of bars and structures of complex shapes were obtained. The maximum solid phase concentration that yielded homogeneous and reasonably

fluent paste was 55 wt%. Dynamic viscosity varied from 1100 to 1250 Pa\*s in these suspensions (Fig. 5A). A further increase of the powders' concentration resulted in the formation of irregular and porous layers during the printing.

Analyses of bending strength of the printed bars from pure M1 and powder-load suspension samples indicated the absence of a worsening of mechanical properties. For instance, the strength of 3YSZ-1 and 3YSZ-2 was 80–90 MPa and was higher than that of the M1 polymer

**Table 2**  
Viscosity of different suspension load and pure polymers.

Composition, wt%			$\eta$ , mPa*s	$\tau_{r=0}$ , Pa
AC	M1	M1+3YSZ-1		
100	0	0	16±1	0.16±0.15
0	100	0	116±1	-0.44±0.84
0	78	22	215±1	-1.60±0.58
0	59	41	635±4	0.12±1.17
0	54	46	1079±4	0.77±0.73
0	49	51	1218±8	1.27±1.27

(45–50 MPa), which meant good adhesion of the ceramic particles to the polymer matrix.

### 3.5. The 3D printed samples' properties

To optimize the debinding process, a DTA/TG analysis of the printed samples was performed. Two types of samples were prepared with similar powder loading: samples with 50 wt% of 3YSZ-1 based on either custom-designed photopolymer resin M1 or purchased photopolymer resin AC. Mass loss at constant heating (10 °C/min) and thermal effects were investigated in air and N<sub>2</sub> streams. The results are presented in Fig. 6A. The mass loss in all samples started at ~220 °C. The maximum mass loss occurred in the 370–420 °C temperature range. In the inert atmosphere, the mass loss was complete at 500 °C for both photopolymers. Approximately 10 wt% of polymers' mass remained in the samples in the form of carbon black, as confirmed by the color of the samples after the tests. In the case of the air atmosphere, the polymers' behavior at the last stage of the burning out was different. The 50% mass loss of the samples confirmed that M1 was completely removed at 600 °C, whereas AC got burned out at 650 °C. The samples were white and carbon black was not detectable visually. We observed an exothermic effect during the heating in the air stream for both polymers. In accordance with the mass loss data, the AC polymer's peak got shifted toward a higher temperature by 50 °C. A low-intensity endothermic effect was observed for both samples during the heating in the nitrogen stream at the high temperature owing to sublimation of the thermally destroyed polymers.

At the same time, the heating in the air stream gave rise to cracks.

Judging by the DTA/TG data, a debinding mode of M1 in nitrogen was devised for the removal of the polymers without sample cracking (Fig. 6B). The samples were heated at different rates, and the emergence of cracks was checked. The heating for 24 h up to 220 °C ensured preservation of the sample's shape and did not cause cracks, whereas an increase in the heating rate resulted in the cracks (blue point). Further heating up to 260 °C was implemented during 58 h, and then the samples were additionally heated up to 300 and 360 °C during 18 and 42 h, respectively. The higher heating rate at high temperature also led to cracks. Thus, up to 91 wt% of the polymer was removed in the newly developed mode, and the 9% of the preserved mass could be attributed to the formed carbon black and traces of the polymer.

The linear shrinkage during the heating of 3YSZ-1 printed with AC and M1 samples was investigated too (Fig. 6D). According to the results, the samples after debinding are characterized by the onset of the shrinking, and the M1 polymer caused a 5% higher shrinkage value as compared to the AC sample. After the heating up to 1500 °C, the shrinkage of the M1-based sample reached 41%, whereas in the AC-based one, the shrinkage did not exceed 35%. Thus, the more noticeable shrinkage during the debinding led to closer fitting of particles in the sample, thereby resulting in more intense sintering during the subsequent high-temperature procedures.

### 3.6. Properties of the 3D-printed sintered samples

On the basis of the data obtained in subsections 3.2 and 3.5, the 3D

printed samples of 3YSZ-1 and 3YSZ-2 ceramics were heat-treated. Before sintering, M1 was removed according to the newly developed debinding mode. After the debinding, the ceramics were sintered at 1600 °C (3YSZ-1) or 1500 °C (3YSZ-2) for 2 h. The phase composition of the ceramics is presented in Fig. 6E. The 3YSZ-1 ceramics are characterized by a high content of the monoclinic phase: up to 33%, whereas the 3YSZ-2 sample retained 100 wt% of t-ZrO<sub>2</sub> (Fig. 6E). The formation of the monoclinic phase was associated with an increase in the sintering temperature.

The microstructure of ceramics 3YSZ-1 and 3YSZ-2 obtained by the DLP method (Fig. 7A) is displayed in Fig. 7B. The ceramic samples showed linear-shrinkage values of 41% and a consolidated microstructure with local pore spaces (Fig. 7C, 7Cf) for both compositions. 3YSZ-1 manifested well-pronounced layer boundaries and transverse cracks that formed during printing and sintering [34], in contrast to the 3YSZ-2 material (Fig. 7Ca,7Cb). Sample 3YSZ-2 is characterized by blurring, up to disappearance of the boundaries between the layers (Fig. 7Cd, 7Ce).

Bending strength of 3YSZ-1 samples did not exceed 45 MPa owing to the crack formation and appearance of m-ZrO<sub>2</sub> in the sintered materials. The 3YSZ-2 samples are characterized by 190 MPa bending strength, which is more than 4 times higher than that of 3YSZ-1.

Various details involving CAD-predicted shapes and micro-architectures were fabricated according to the newly developed printing, debinding, and sintering modes. The ceramic details' microarchitecture is characterized by 100 μm thickness of the produced details (model of DNA). The presented digital photographs of sintered 3D objects feature the absence of transverse cracks in the 3YSZ-2 samples in contrast to 3YSZ-1 samples (Fig. 7C).

### 3.7. Cytocompatibility of the zirconium-containing ceramics

According to the results of the assays of the ceramic samples, the samples of zirconium-containing ceramics are not toxic to MG-63 cells. Optical density of the formazan solution for the test samples of materials either did not differ significantly from the control (days 1 and 6 of observation) or statistically significantly exceeded the control values (day 4 experiment), i.e., the proliferation rate was almost identical between cells growing on polystyrene culture plastic and cells growing on samples of zirconium-containing ceramics in the course of the experiment. All of the above was also confirmed by the PVC for the prototype ceramic samples during the experiment (Table 3) and by micrographs of MG-63 cells in the control (on plastic) and on samples of zirconium-containing ceramics (Fig. 7D).

Overall, the *in vitro* findings indicated the cytocompatibility of the newly developed zirconium-containing ceramics.

### 3.8. In vivo results

#### 3.8.1. In vivo experiments with the decalcified samples

In this study, we present for the first time the results of *in vivo* implantation of a ZrO<sub>2</sub>-based DLP-produced ceramic (Fig. 8). The 3YSZ-1 material was chosen based on the above *in vitro* findings.

According to results on the extracted and decalcified samples, after 4 weeks of the examination, the bone defect was closed from the outside by a connective tissue ridge (Fig. 8A). The edges of the defect after the removal of the implant were represented by almost parallel stripes of a dense compact bone area. No signs of inflammation were found. At the bone-implant interface along the edge of the bone defect, cell chains of osteoblasts were found, pointing to a tight fit of the 3D implant to the bone in the defect and the beginning of osseointegration.

In the control group, the process of reparative osteogenesis proceeded without the use of osteoplastic materials, under a blood clot. It was found that during this period, the area of the defect got covered by loose multilayer connective tissue, and no signs of consolidation of bone fragments were found (Fig. 8B).

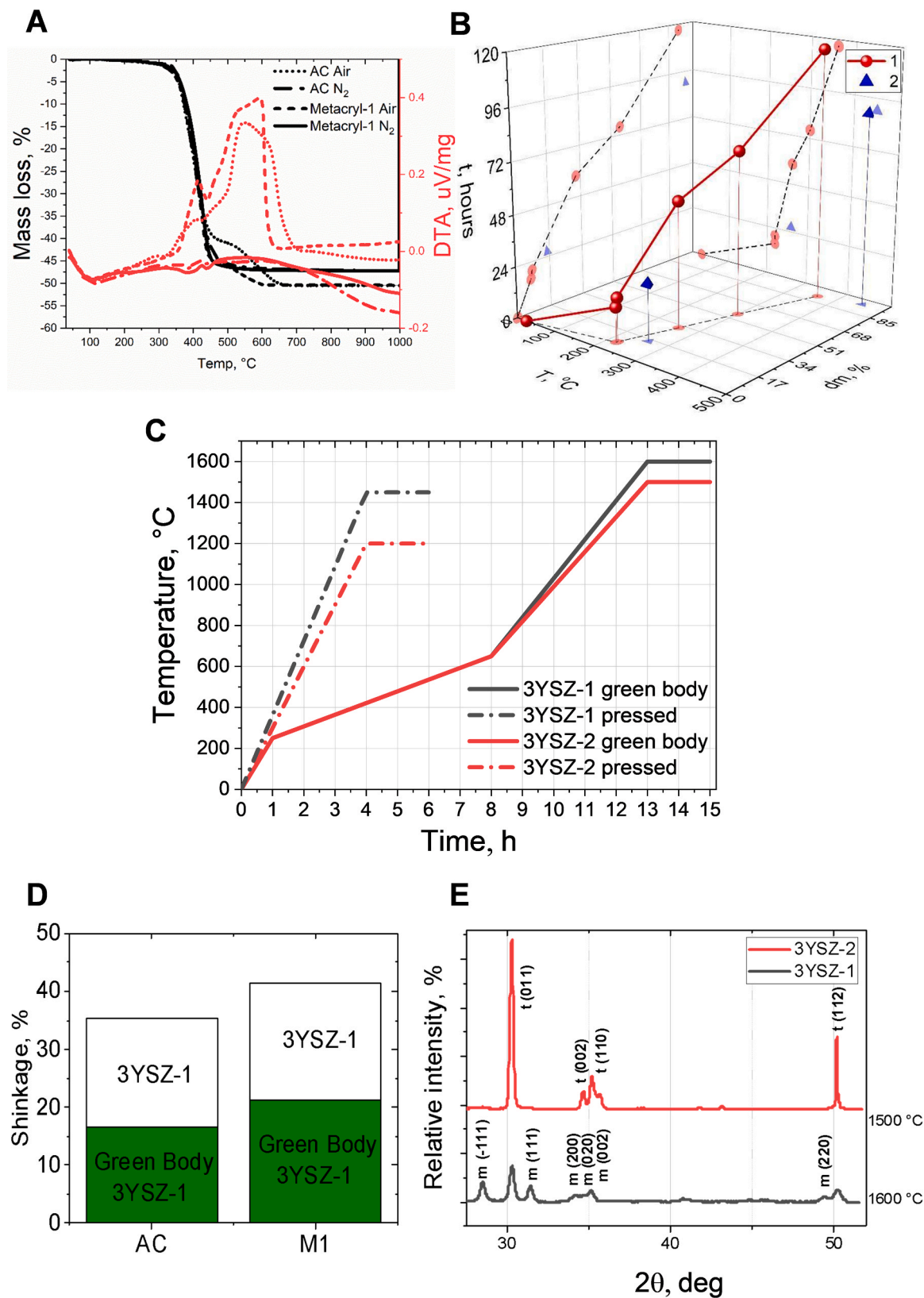


**Fig. 6.** A: DTA/TG analysis of printed samples based on polymer M1 or AC in air or nitrogen (50% by weight of photopolymer resin). B: The debinding curve dependence of the M1 polymer's mass loss (dm, %) on temperature and time for samples containing 50% ZrO<sub>2</sub> in a nitrogen atmosphere. 1: samples without cracks, 2: samples with cracks after the heat treatment. C: Sintering curves for pressed samples (solid lines) and samples after debinding (green bodies) (dash-dot lines) on air. D: Effect of the polymer type on shrinkage of green bodies and sintered samples. 34%/22% residual open porosity. E: XRD analysis of sintered samples after 3D printing. m: m-ZrO<sub>2</sub>, t: t-ZrO<sub>2</sub>.

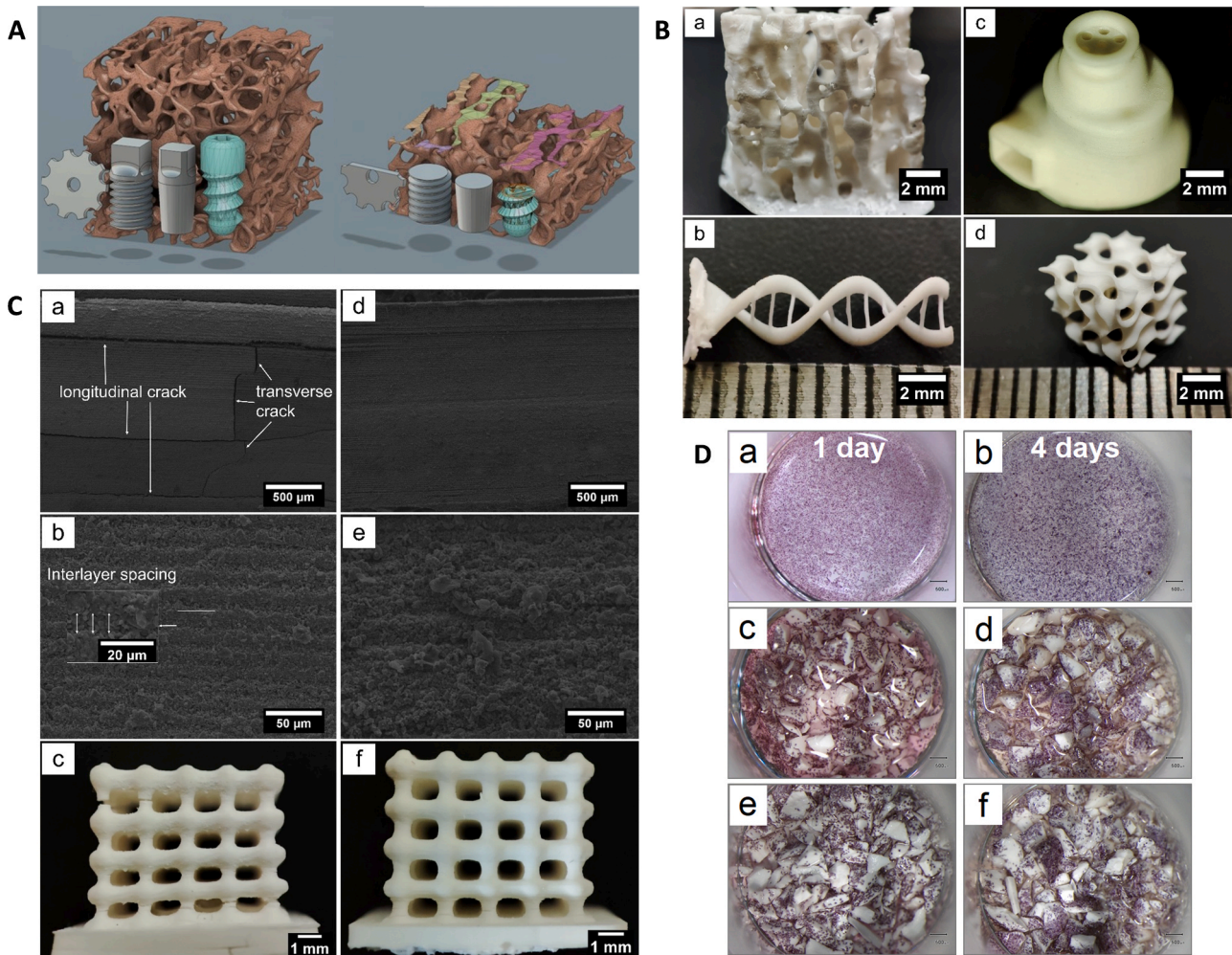


**Fig. 7.** A: Scheme of the DLP part construction. B: Macro photographs of sintered 3D objects of complex geometric shapes containing a liquid phase additive, where a - a fragment of bone structure, b - a model of a DNA molecule with strands 200  $\mu\text{m}$  thick, c - the body of an earphone, d - a gyroid. C: Macro- and microstructural images of sintered 3D objects, where a, b, c: 3YSZ-1 (1600  $^{\circ}\text{C}$ ) and d, e, f: 3YSZ-2 (1500  $^{\circ}\text{C}$ ). D: Cultivation of human osteosarcoma MG-63 cells on polystyrene (a, b: control), 3YSZ-1 (c, d), or 3YSZ-2 (e, f) in the course of observation. a, c, e: day 1, and b, d, f: day 4. MTT assay, magnification 20 $\times$ .

**Table 3**

Optical density (OD) of the formazan solution (MTT assay) and the PVC during MG-63 cell growth on polystyrene (control) or on samples of zirconium-containing ceramics as a function of time.

N $^{\circ}$ No.	Samples	OD (arb. units) and PVC (in % of control) at several time points			
		Observation duration	1 day	4 days	6 days
	Control (polystyrene)		0.517 $\pm$ 0.003 100.0%	0.782 $\pm$ 0.007 100.0%	1.057 $\pm$ 0.041 100.0%
1	ZrO $_2$		0.517 $\pm$ 0.002 100.0%	0.864 $\pm$ 0.003* 110.5%	1.064 $\pm$ 0.043 100.7%
2	ZrO $_2$ +Na $_2$ Si $_2$ O $_5$		0.516 $\pm$ 0.010 99.8%	0.901 $\pm$ 0.005* 115.2%	1.054 $\pm$ 0.037 99.7%

\* A significant difference from the control according to Student's *t* test ( $p < 0.05$ )

### 3.8.2. In vivo investigation of the samples fabricated by means of the precision device

Microscopic examination of the bone sections revealed that the intraosseous implant was located inside the diaphysis of the rat tibia and was passing through the cortical plate, the medullary canal, and partially through the contralateral cortical plate (Fig. 8D). The bone tissue surrounded the implant on all sides, including the area of the implant surface facing the bone marrow canal.

In the morphometric analysis, the contact of the bone with the surface of the implant proved to be 97.3%. At the same time, the 2.7% of the area of unoccupied bone tissue was in contact with the reticular stroma of bone marrow. A fibrous tissue was not detectable. Thus, the results indicated good osteointegration.

## 4. Discussion

This paper presents effects of the Na $_2$ Si $_2$ O $_5$  additive on the ZrO $_2$  ceramics produced by cold pressing or DLP printing from nanopowders obtained via the precipitation route. The newly developed nanopowders are characterized by higher sintering activity as compared to commercially available ZrO $_2$ -based powders [35]. The ceramic without the silicate additive—3YSZ-1—when sintered even at 1350  $^{\circ}\text{C}$  showed a bending strength of 681  $\pm$  25 MPa, which is higher than that of 3Y-TZP tested by the Song et al. [36]. The observed ceramic microstructure features the presence of grains with a size of 200 nm, which contribute to the good mechanical properties. A further increase in the sintering temperature or in holding time resulted in the grains' growth and a reduction in the strength.

The addition of Na $_2$ Si $_2$ O $_5$  (resulting in 3YSZ-2) did not affect noticeably the powder's surface area but led to a significant decrease in the sintering temperature, preservation of the t-ZrO $_2$  phase (Fig. 1C), and formation of fine microstructure (Fig. 3A). We observed a uniform

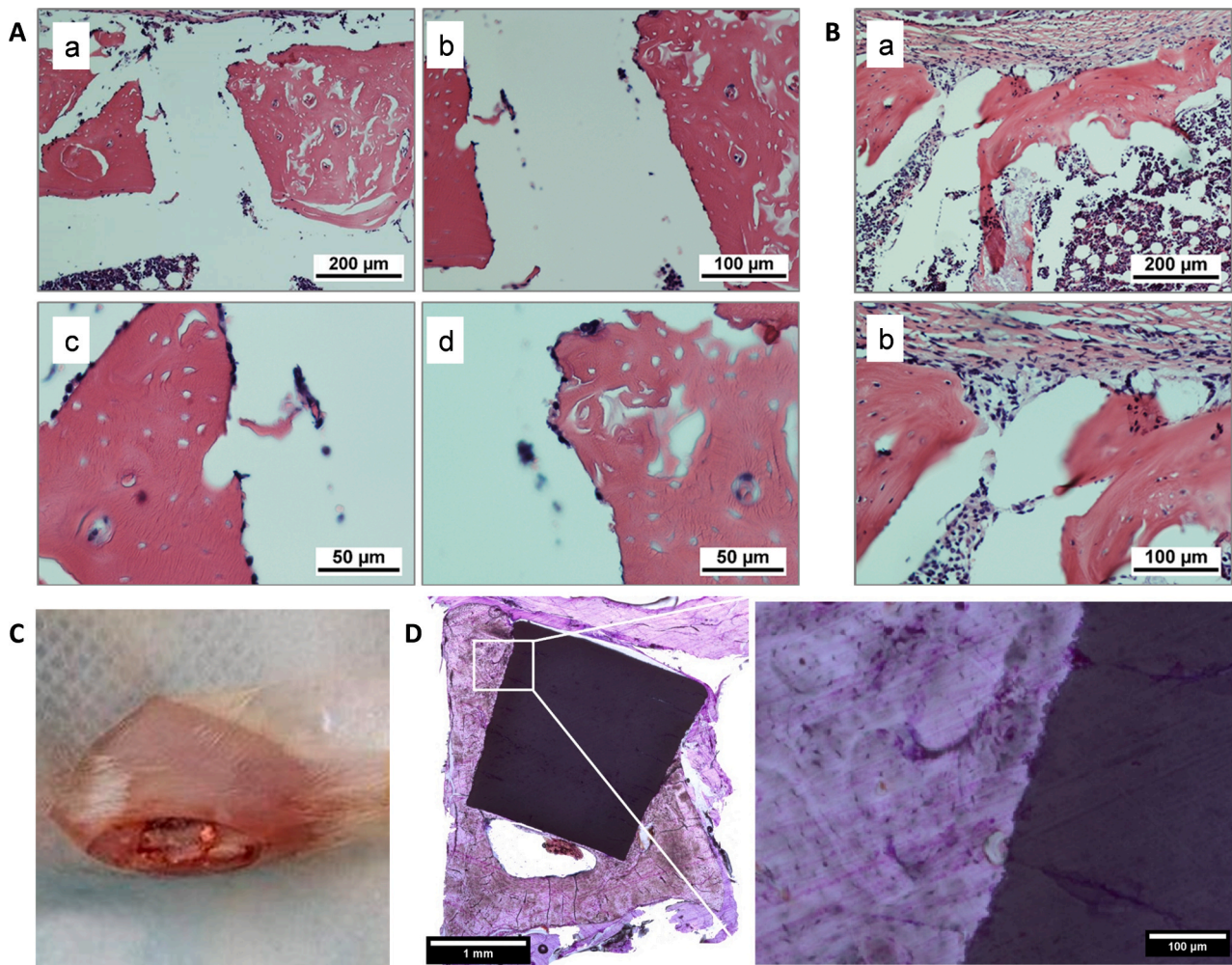


**Fig. 8.** A: Histological analysis of the rat tibia defect after extraction of the 3D printed  $ZrO_2$  ceramic at 4 weeks after implant placement in the bone defect. H&E staining. B: Histological analysis of the rat tibia defect in a control (closure under a blood clot) at 4 weeks after the surgical procedure. H&E staining. C: Filling of the rat tibia bone defect with an implant. D: Microscopic examination of the bone sections.

distribution of the silicate additive along grain boundaries (Fig. 3C) [32, 33].

We suppose that the introduction of  $Na_2Si_2O_5$  led to the formation of a liquid phase [37], as evidenced by noticeably greater shrinkage according to dilatometric data (Fig. 2A). Open porosity lower than 1% was reached at 1200 °C. To the best of our knowledge, this low temperature is a major achievement in  $ZrO_2$  ceramic technology. For example, high-density materials with appropriate bending strength have been obtained by liquid-phase sintering at 1400 °C using a  $CaO-Al_2O_3-SiO_2$  additive in 3Y-TZP [38,39]. Only in the presence of cerium was a relatively low sintering temperature (1250–1400 °C) effective for 3Y-TZP/12Ce-TZP with 1 wt% of  $MgO-Al_2O_3-SiO_2$  glass [40]. Only with an extremely high percentage of  $SiO_2$  glass—up to 35 mol.% in the raw materials—was diminution of sintering temperature down to 1170 °C reached for a  $ZrO_2-SiO_2$  material obtained by spark plasma sintering [41,42].

In our work, the 3YSZ-2 ceramics were formed only by the t- $ZrO_2$  crystalline phase across the entire range of sintering temperatures (1100–1250 °C), and bending strength reached  $450 \pm 25$  MPa at 1200 °C. Lower strength of 3YSZ-2 ceramics during the sintering above 1250 °C was due to the presence of a low-strength sodium disilicate melt along grain boundaries, where the fracture occurred, according to the TEM data (Fig. 3C) [43]. On the other hand, in comparison with ceramics without additives, the increase in strength was 56% at 1150 °C. Thus, in the low-temperature sintering range up to 1250 °C, the presence of a

melt significantly intensifies the sintering and enhances the mechanical characteristics.

The application of  $ZrO_2$  nanopowders for manufacturing DLP additives is a promising way to improve the properties of ceramic parts [35]. In our work, we applied a custom-made photopolymer resin based on methacrylate, which is appropriate for nanopowder-based slurry preparation. The introduction of 50 wt% of the solid phase still allowed to produce a green body on a commercially available 3D DLP printer, which was originally designed for pure low-viscosity photopolymers. Compared with the photopolymer resin from the commercial source (AC), the composition developed by us is characterized by lower debinding temperatures in an  $N_2$  atmosphere. We noticed a significant improvement of the quality of printed green bodies and sintered ceramic samples (Fig. 9).

At the same time, a strong influence of the ceramic powders' composition on properties of printed and sintered samples was observed. The 3YSZ-2 products manifested improved geometrical characteristics transaction during the printing and were found to be resistant to cracking during the heating, when debinding and sintering were performed (Fig. 7C).

The introduction of  $Na_2Si_2O_5$  protected the materials from cracking during the debinding of the 3D printed green bodies but did not affect photopolymer resin viscosity and slurry properties. For successful printing by the DLP method, it is necessary to obtain a suspension with certain acceptable dynamic viscosity and sedimentation stability. These

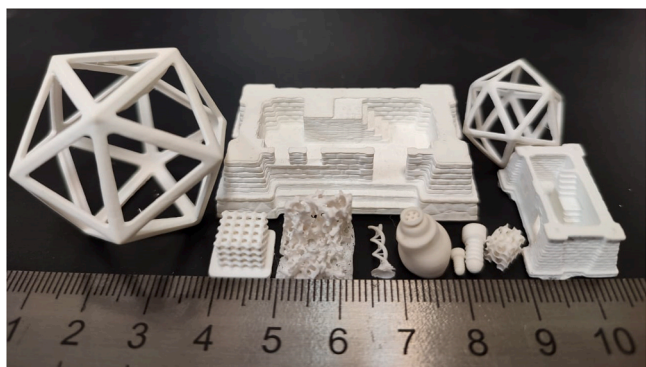


Fig. 9. A general view of our 3D objects in a variety of shapes and sizes.

parameters are highly dependent on particle size and powder density. At the same time, for successful sintering of green bodies, it is necessary to maximize the number of powder particles with the photopolymer to avoid deformations and cracks. Therefore, it is essential either to stir/apply the suspension mechanically layer by layer, as performed on the Lithoz highly expensive equipment [44], or diminish suspension viscosity via a decrease in the concentration of ZrO<sub>2</sub> particles. If the viscosity of the suspension rose above 1200 mPa·s, then printing failed. Based on the change in dynamic viscosity, composition with the maximum proportion of ceramic powder in the photopolymer resin was reached: 50–55 wt% (Fig. 5A), corresponding to 0.9–1.1 g of the powder per milliliter of the suspension. These concentrations gave sedimentation stability (Fig. 5D). With a higher concentration, sedimentation stability increased, and a significant difference was observed after the introduction of more than a 50% proportion of the powder. The highest proportion ensuring the fluidity of the suspension was 67 wt% (only for printers with a squeegee); in this case, the suspension had sedimentation stability for more than 1 week [45].

DTA/TG data showed that the custom-designed polymer Metacryl-1 (M1) has a lower pyrolysis onset temperature as compared to AnyCubic Basic Clear (AC). The presence of an oxidizing agent (air) also lowered the mass loss onset temperature, indicating the presence of oxidation processes that led to the release of CO<sub>2</sub> and, as a consequence, disruption of the product's structure (Fig. 6A). As compared to the purchased polymer AC, we observed a better effect of polymer M1 in samples without the silicate additive (3YSZ-1) on the volumetric shrinkage of samples at the stage of debinding up to 360 °C (16% for AC and 21% for M1) and at the stage of sintering at 1500 °C (35% for AC and 41% for M1) (Fig. 6D). This also affects final density of the product and improves its strength characteristics; the samples had an open porosity of 34% (for AC) and 22% (for M1). Therefore, the pre-shrinkage of the polymer in the debinding process increases the sintering activity of the ceramic owing to higher density of the green body and reduces the probability of cracking [46,47]. In ref. [46], 3D printer AutoceraM (Beijing Ten Dimensions Technology Co., Ltd) was used for printing, and this printer was developed for printing from ceramic suspensions and has a relatively high price compared to well-known brands (Lithoz and Ceramaker) but allows to employ highly viscous pastes with a high percentage of the filling with the powder particles relative to the photopolymer resin. For α-Al<sub>2</sub>O<sub>3</sub>, those authors give the ratio of 495 g of powder per 100 g of resin. The debinding process took place from 6 to 16 h, while the shrinkage was uneven along different axes (x, y, z), indicating irregular stripping in an inert atmosphere when a photosensitive resin is used (Al100-1, Beijing Ten Dimensions Technology Co., Ltd.). The photosensitive resin M1 prepared in our work, owing to its shrinkage properties, allows to apply low-viscosity fluid suspensions in commercially available printers that are not equipped with a stirring squeegee device, for example, Anycubic Photon S (<https://www.anycubic.com/products/anycubic-photon-s>), intended for printing exclusively with resins without a filler. On the other hand, it is necessary to perform

a very prolonged debinding process (up to 120 h) at low temperatures (up to 360 °C). It is possible to speed up the stripping process by using low vacuum in the tube furnace chamber [48]. Fig. 6B depicts the dependence of the weight loss over time on temperature. Note the two red dots at 220 °C. Both points were at the same temperature, but one of the points involved a 0.7% greater weight loss after holding for 4 h. With further heating, the probability of the cracking decreased, in the case of longer exposure at the previous point. For example, two blue dots are presented, which describe the presence of cracks in a given range of temperature, time, and weight loss. Thus, to preserve the geometry and structure without cracks and deformations, elongated isothermal holding and smooth distillation of the polymer are required. As a result of long exposure at low temperatures, more volatile substances are first distilled off and residual stresses are removed [49–51]. Small channels for gas removal arise, through which the bulk of the photopolymer is subsequently distilled off [12]. The achieved printing accuracy on budget DLP equipment is without a precedent. The most of the presented results on the ZrO<sub>2</sub> DLP printed and sintered samples were obtained by commercial industrial printers. Also, most of commercially available ceramic suspension for printing are sold as suspensions adapted for use on only same-branded expensive industrial 3D printers. In our paper we applied a table photopolymer printer and developed the ceramic suspension, which are affordable for dental clinics and a wide range of consumers. The obtained results demonstrated the opportunity to produce the ceramic parts comparable with the materials, which were obtained by the commercial CeraFab 7500 (Lithoz, Austria). The zirconia suspension consists of tetragonal zirconia polycrystal “LithaCon 3Y 610 Purple” previously was demonstrated for printing and sintering of the part with a high precision of the product [52,53]. The powder synthesis methods and rigorous components of the resin are not published. Bergler et al. presented the results of the flexural strength measurement of the commercial 3D-printed 3 mol.% yttria-stabilized zirconia (LithaCon 3Y 230, Lithoz) which reached of 855.4 ± 112.6 MPa [54]. However, the both papers did not mention the 3D printers which were applied in the papers. Komissarenko et al. presented the results of high precision printing of the samples of scandia-stabilized zirconia ceramics using an affordable photopolymer 3D printer, Ember (Autodesk, USA) [55]. The tetragonal ZrO<sub>2</sub> powders were produced by JSC “Neochem” using the co-precipitation method from concentrated aqueous solutions of zirconium oxychloride, scandium and yttrium nitrates, and ammonia, followed by annealing at 900 °C. However, the flexural strength was not presented. In ref. [45], researchers managed to obtain 3D objects by similar SLA methods; however, the parts did not have high precision and print resolution and had simple geometric shapes. In ref. [56], high-resolution objects are presented, but a 3D printer is not specified. In another work [8], similar compositions of ceramic ZrO<sub>2</sub> powders are presented, and the absence of cytotoxicity is demonstrated; samples in the form of teeth were printed on a dental 3D printer.

In our article, we demonstrated that the obtained materials are nontoxic and cytocompatible with the MG-63 cell line. Additionally, for the first time (to the best of our knowledge), the ZrO<sub>2</sub> DLP-printed parts were investigated *in vivo* via implantation into a bone defect. Previously, ZrO<sub>2</sub> DLP-printed ceramics have shown cytocompatibility with rBMSC cells [8]. Data from *in vivo* studies on ceramics based on ZrO<sub>2</sub> are limited and mainly consist of results about composite materials [57,58]. In our paper, we demonstrate tight contact between a DLP-printed sintered implant and a bone tissue. Thus, the presented technology helped to obtain cyto- and biocompatible ZrO<sub>2</sub> bone implants with pronounced osseointegrative properties.

## 5. Conclusion

In this paper, 3YSZ nanopowders were synthesized via a precipitation method. The introduction of a sodium disilicate additive resulted in the formation of a liquid phase and significant intensification of sintering processes. Dense ceramic parts with an open porosity of less than

1% and a bending strength of 360 MPa were sintered at 1150 °C. The synthesized 3YSZ powders and custom-made photopolymer resin based on methyl methacrylate were applied to the preparation of a slurry for printing on a low-cost 3D DLP printer (from a commercial source), which was originally designed for pure low-viscosity photopolymers. The newly developed debinding mode and sintering procedures yielded ceramic parts with complex shapes and predicted porosity. The sodium disilicate additive improved resistance to cracking owing to the presence of a liquid phase and better shrinkage during debinding. These effects prevented transverse cracking and led to predicted transformations of geometrical characteristics. The presented low strength is due to the glass phase based on the sintering additive sodium disilicate ( $\text{Na}_2\text{O} - 2\text{SiO}_2$ ), formed along the grain boundaries. The additive reduced the sintering temperature, but the strength diminished too. According to an *in vitro* test on the MG-63 cell line, the newly developed ceramic materials are not cytotoxic. Additionally, the biocompatibility and osseointegrative abilities of the 3D printed  $\text{ZrO}_2$  parts were demonstrated in a rat model of a tibia bone defect. The proposed approach holds promise for the production of dental and surgical medical parts for personalized medicine.

### Declaration of Competing Interest

All authors declare that there are no competing interests.

### Data availability

No data was used for the research described in the article.

### Acknowledgments

This work was carried out with the support of A.A. Baikov Institute of Metallurgy and Materials Science, Russian Academy of Sciences State assignment No. 075-00320-24-00. The authors are also grateful for the financial support from the Government (CITIS No. 121031300084-1) for viscosity and sedimentation stability studies. This work was performed using the equipment of the Core Facilities Center of IPCE RAS (CKP FMI IPCE RAS). The English language was proofread by shevchuk-editing.com.

### References

- C. Gautam, J. Joyner, A. Gautam, J. Rao, R. Vajtai, Zirconia based dental ceramics: structure, mechanical properties, biocompatibility and applications, *Dalton Trans.* (2016), <https://doi.org/10.1039/c6dt03484e>.
- A. Suresh, M.J. Mayo, W.D. Porter, Thermodynamics of the tetragonal-to-monoclinic phase transformation in fine and nanocrystalline yttria-stabilized zirconia powders, *J. Mater. Res.* (2003), <https://doi.org/10.1557/JMR.2003.0406>.
- A. Suresh, M.J. Mayo, W.D. Porter, C.J. Rawn, Crystallite and grain-size-dependent phase transformations in yttria-doped zirconia, *J. Am. Ceram. Soc.* (2003), <https://doi.org/10.1111/j.1151-2916.2003.tb00025.x>.
- M. Trunec, Effect of grain size on mechanical properties of 3Y-TZP ceramics, *Ceramics - Silikaty* (2008).
- L.B. Silva, W. Acchar, V.M. Silva, Study of the sintering dental ceramic waste from  $\text{ZrO}_2\text{-Y}_2\text{O}_3$  system, *Mater. Sci. Forum* (2017), <https://doi.org/10.4028/www.scientific.net/MSF.881.392>.
- Z. Chen, Z. Li, J. Li, C. Liu, C. Lao, Y. Fu, C. Liu, Y. Li, P. Wang, Y. He, 3D printing of ceramics: a review, *J. Eur. Ceram. Soc.* (2019), <https://doi.org/10.1016/j.jeurceramsoc.2018.11.013>.
- M. Pagac, J. Hajnys, Q.P. Ma, L. Jancar, J. Jansa, P. Stefek, J. Mesicek, A review of vat photopolymerization technology: materials, applications, challenges, and future trends of 3d printing, *Polymers (Basel)* (2021), <https://doi.org/10.3390/polym13040598>.
- F. Chen, H. Zhu, J.M. Wu, S. Chen, L.J. Cheng, Y.S. Shi, Y.C. Mo, C.H. Li, J. Xiao, Preparation and biological evaluation of  $\text{ZrO}_2$  all-ceramic teeth by DLP technology, *Ceram. Int.* (2020), <https://doi.org/10.1016/j.ceramint.2020.01.152>.
- J. Zhang, L. Wei, X. Meng, F. Yu, N. Yang, S. Liu, Digital light processing-stereolithography three-dimensional printing of yttria-stabilized zirconia, *Ceram. Int.* (2020), <https://doi.org/10.1016/j.ceramint.2019.12.113>.
- J. Sun, H. Gu, J. Jiang, Y. Xu, B. Li, J. Zhang, Study on forming accuracy of  $\text{ZrO}_2$  ceramic materials prepared by DLP technology, *IOP Conf. Ser. Earth Environ. Sci.* (2021) 32006.
- K. Zhang, R. He, G. Ding, C. Feng, W. Song, D. Fang, Digital light processing of 3Y-TZP strengthened  $\text{ZrO}_2$  ceramics, *Mater. Sci. Eng. A* (2020), <https://doi.org/10.1016/j.msea.2019.138768>.
- K. Wang, M. Qiu, C. Jiao, J. Gu, D. Xie, C. Wang, X. Tang, Z. Wei, L. Shen, Study on defect-free debinding green body of ceramic formed by DLP technology, *Ceram. Int.* (2020), <https://doi.org/10.1016/j.ceramint.2019.09.237>.
- M. Zhou, W. Liu, H. Wu, X. Song, Y. Chen, L. Cheng, F. He, S. Chen, S. Wu, Preparation of a defect-free alumina cutting tool via additive manufacturing based on stereolithography - optimization of the drying and debinding processes, *Ceram. Int.* (2016), <https://doi.org/10.1016/j.ceramint.2016.04.050>.
- H. Wu, Y. Cheng, W. Liu, R. He, M. Zhou, S. Wu, X. Song, Y. Chen, Effect of the particle size and the debinding process on the density of alumina ceramics fabricated by 3D printing based on stereolithography, *Ceram. Int.* (2016), <https://doi.org/10.1016/j.ceramint.2016.08.024>.
- S. Tekeli, M. Erdogan, B. Aktas, Microstructural evolution in 8 mol%  $\text{Y}_2\text{O}_3$ -stabilized cubic zirconia (8YSZ) with  $\text{SiO}_2$  addition, *Mater. Sci. Eng. A* (2004), <https://doi.org/10.1016/j.msea.2004.07.057>.
- S. Aravindan, R. Krishnamurthy, Joining of ceramic composites by microwave heating, *Mater. Lett.* (1999), [https://doi.org/10.1016/S0167-577X\(98\)00166-9](https://doi.org/10.1016/S0167-577X(98)00166-9).
- V.V. Smirnov, S.V. Smirnov, T.O. Obolkin, O.S. Antonova, M.A. Goldberg, D. R. Khairutdinova, O.A. Ovchinnikova, S.M. Barinov, Sintering and properties of dioxides of ceramics containing the sodium silicate additive, *Доклады Академии Наук* (2019), <https://doi.org/10.31857/s0869-5652488136-39>.
- V.V. Smirnov, S.V. Smirnov, T.O. Obolkin, O.S. Antonova, M.A. Gol'dberg, D. R. Khairutdinova, O.A. Ovchinnikova, S.M. Barinov, Effect of sodium silicate on the sintering and properties of zirconia ceramics, *Dokl. Chem.* (2019), <https://doi.org/10.1134/S0012500819090015>.
- V.V. Smirnov, S.V. Smirnov, T.O. Obolkin, O.S. Antonova, M.A. Goldberg, S. M. Barinov, Low-temperature liquid-phase sintering of zirconia: phase composition and microstructure, *Dokl. Chem.* (2020), <https://doi.org/10.1134/S0012500820100043>.
- Z. Wu, W. Liu, H. Wu, R. Huang, R. He, Q. Jiang, Y. Chen, X. Ji, Z. Tian, S. Wu, Research into the mechanical properties, sintering mechanism and microstructure evolution of  $\text{Al}_2\text{O}_3\text{-ZrO}_2$  composites fabricated by a stereolithography-based 3D printing method, *Mater. Chem. Phys.* (2018), <https://doi.org/10.1016/j.matchemphys.2017.12.021>.
- V.V. Smirnov, S.V. Smirnov, A.I. Krylov, O.S. Antonova, M.A. Goldberg, L. I. Shvorneva, D.D. Titov, L. Medvecky, A.S. Baikin, S.M. Barinov, Ceramics based on zirconia with a low sintering temperature, *Powder Metall. Prog.* 14 (2014) 148–156.
- S.S. Kim, T.H. Sanders, Thermodynamic modeling of phase diagrams in binary alkali silicate systems, *J. Am. Ceram. Soc.* 74 (1991) 1833–1840, <https://doi.org/10.1111/j.1151-2916.1991.tb07796.x>.
- V.V. Smirnov, A.I. Krylov, S.V. Smirnov, M.A. Goldberg, O.S. Antonova, L. I. Shvorneva, S.M. Barinov, Study of liquid-phase sintering of materials based on zirconium dioxide containing alumina, *Inorg. Mater.: Appl. Res.* 8 (2017), <https://doi.org/10.1134/S2075113317010373>.
- V.V. Smirnov, S.V. Smirnov, T.O. Obolkin, O.S. Antonova, M.A. Gol'dberg, D. R. Khairutdinova, O.A. Ovchinnikova, S.M. Barinov, Effect of sodium silicate on the sintering and properties of zirconia ceramics, *Dokl. Chem.* 488 (2019) 239–241, <https://doi.org/10.1134/S0012500819090015/FIGURES/2>.
- J. D'Ans, J. Löffler, Untersuchungen im system  $\text{Na}_2\text{O-SiO}_2\text{-ZrO}_2$ , *Z. Anorg. Allg. Chem.* 191 (1930) 1–35, <https://doi.org/10.1002/zaac.19301910102>.
- M. Klinger, More features, more tools, more CrysTBox, *J. Appl. Crystallogr.* 50 (2017) 1226–1234, <https://doi.org/10.1107/S1600576717006793>.
- M. Goldberg, T. Obolkin, S. Smirnov, P. Protsenko, D. Titov, O. Antonova, A. Konovalov, E. Kudryavtsev, I. Sviridova, V. Kirsanova, N. Sergeeva, V. Komlev, S. Barinov, The influence of co additive on the sintering, mechanical properties, cytocompatibility, and digital light processing based stereolithography of 3y-tzp-5al2 o3 ceramics, *Materials* (2020), <https://doi.org/10.3390/ma13122789>.
- H. Li, Y.S. Liu, Y.S. Liu, Q.F. Zeng, K.H. Hu, J.J. Liang, Z.G. Lu, Microstructure and properties of 3D-printed alumina ceramics with different heating rates in vacuum debinding, *Rare Met.* (2020), <https://doi.org/10.1007/s12598-020-01372-x>.
- K. Maca, M. Trunec, R. Chmelik, Processing and properties of fine-grained transparent  $\text{MgAl}_2\text{O}_4$  ceramics, *Ceramics - Silikaty* (2007).
- T. Mosmann, Rapid colorimetric assay for cellular growth and survival: Application to proliferation and cytotoxicity assays, *J. Immunol. Methods* (1983), [https://doi.org/10.1016/0022-1759\(83\)90030-4](https://doi.org/10.1016/0022-1759(83)90030-4).
- A.V. Volkov, B.S. Smbatyan, D.N. Nazaryan, A.A. Muraev, A novel morphometric nomenclature to evaluate osseointegration of intrasosseous implants, *Sovrem. Tehnol. V. Med.* (2018), <https://doi.org/10.17691/stm2018.10.3.1>.
- M. Isaacson, M. Ohtsuki, M. Utlaut, *Electron microscopy of individual atoms. in: Introduction to Analytical Electron Microscopy*, Springer, 1979, pp. 343–368.
- D.E. Jesson, S.J. Pennycook, Incoherent imaging of crystals using thermally scattered electrons, *Proc. R. Soc. A: Math. Phys. Eng. Sci.* (1995), <https://doi.org/10.1098/rspa.1995.0044>.
- E. Johansson, O. Lidström, J. Johansson, O. Lyckfeldt, E. Adolfsson, Influence of resin composition on the defect formation in alumina manufactured by stereolithography, *Materials* (2017), <https://doi.org/10.3390/ma10020138>.
- Y. Li, M. Wang, H. Wu, F. He, Y. Chen, S. Wu, Cure behavior of colorful  $\text{ZrO}_2$  suspensions during Digital light processing (DLP) based stereolithography process, *J. Eur. Ceram. Soc.* 39 (2019) 4921–4927.
- Y. Song, D. Zhu, J. Liang, X. Zhang, Enhanced mechanical properties of 3  $\text{Y}_2\text{O}_3$  stabilized tetragonal  $\text{ZrO}_2$  incorporating tourmaline particles, *Ceram. Int.* (2018), <https://doi.org/10.1016/j.ceramint.2018.05.217>.

- [37] S.S. Kim, T.H. Sanders, Thermodynamic modeling of phase diagrams in binary alkali silicate systems, *J. Am. Ceram. Soc.* (1991), <https://doi.org/10.1111/j.1151-2916.1991.tb07796.x>.
- [38] Y. hai Sun, Y. feng Zhang, J. kun Guo, Microstructure and bending strength of 3Y-TZP ceramics by liquid-phase sintering with CAS addition, *Ceram. Int* (2003), [https://doi.org/10.1016/S0272-8842\(02\)00097-4](https://doi.org/10.1016/S0272-8842(02)00097-4).
- [39] X.W. Huang, J.C. Yu, Q. Li, X.D. Huang, X.Q. Li, X.L. Liu, Microstructure and mechanical properties of 3Y-TZP/Al<sub>2</sub>O<sub>3</sub> composites fabricated by liquid phase sintering, *J. Mater. Sci.* (2005), <https://doi.org/10.1007/s10853-005-0671-2>.
- [40] H. Qin, X. Huang, Microstructure and bending strength of 3Y-TZP/12Ce-TZP ceramics fabricated by liquid-phase sintering at low temperature, *J. Am. Ceram. Soc.* (2000), <https://doi.org/10.1111/j.1151-2916.2000.tb01653.x>.
- [41] L. Fu, H. Engqvist, W. Xia, Highly translucent and strong ZrO<sub>2</sub>-SiO<sub>2</sub> nanocrystalline glass ceramic prepared by sol-gel method and spark plasma sintering with fine 3D microstructure for dental restoration, *J. Eur. Ceram. Soc.* 37 (2017) 4067–4081.
- [42] L. Fu, B. Wang, Y. Deng, G. Xu, J. Huang, H. Engqvist, W. Xia, Liquid-phase sintering of ZrO<sub>2</sub>-based nanocrystalline glass-ceramics achieved by multielement co-doping, *J. Am. Ceram. Soc.* (2023), <https://doi.org/10.1111/jace.18945>.
- [43] L. Fu, Y. Wang, L. Riekehr, J. Räthel, H. Engqvist, W. Xia, Observation of yttrium oxide segregation in a ZrO<sub>2</sub>-SiO<sub>2</sub> glass-ceramic at nanometer dimensions, *J. Am. Ceram. Soc.* (2020), <https://doi.org/10.1111/jace.17142>.
- [44] M. Borlaf, N. Szubra, A. Serra-Capdevila, W.W. Kubiak, T. Graule, Fabrication of ZrO<sub>2</sub> and ATZ materials via UV-LCM-DLP additive manufacturing technology, *J. Eur. Ceram. Soc.* (2020), <https://doi.org/10.1016/j.jeurceramsoc.2019.11.037>.
- [45] G. Varghese, M. Moral, M. Castro-García, J.J. López-López, J.R. Marín-Rueda, V. Yagüe-Alcaraz, L. Hernández-Afonso, J.C. Ruiz-Morales, J. Canales-Vázquez, Fabrication and characterisation of ceramics via low-cost DLP 3D printing, *Boletín de La Sociedad Española de Cerámica y Vidrio* (2018), <https://doi.org/10.1016/j.bsevcv.2017.09.004>.
- [46] H. Li, Y. Liu, Y. Liu, Q. Zeng, K. Hu, Z. Lu, J. Liang, Effect of debinding temperature under an argon atmosphere on the microstructure and properties of 3D-printed alumina ceramics, *Mater. Charact.* (2020), <https://doi.org/10.1016/j.matchar.2020.110548>.
- [47] H. Li, Y. Liu, Y. Liu, Q. Zeng, J. Liang, Thermal treatment of  $\gamma$ -Al<sub>2</sub>O<sub>3</sub> for the preparation of stereolithography 3D printing ceramic slurries, *Front. Mater.* (2019), <https://doi.org/10.3389/fmats.2019.00295>.
- [48] Z. Chen, J. Li, C. Liu, Y. Liu, J. Zhu, C. Lao, Preparation of high solid loading and low viscosity ceramic slurries for photopolymerization-based 3D printing, *Ceram. Int.* (2019), <https://doi.org/10.1016/j.ceramint.2019.03.024>.
- [49] M. Podgórski, B.T. Worrell, J. Sinha, M.K. McBride, C.N. Bowman, Thermal metamorphosis in (Meth)acrylate photopolymers: stress relaxation, reshaping, and second-stage reaction, *Macromolecules* (2019), <https://doi.org/10.1021/acs.macromol.9b01678>.
- [50] K.C. Wu, Parametric study and optimization of ceramic stereolithography, *University of Michigan*, 2005.
- [51] A.M. Knapp, J.W. Halloran, Binder removal from ceramic-filled thermoplastic blends, *J. Am. Ceram. Soc.* (2006), <https://doi.org/10.1111/j.1551-2916.2006.01179.x>.
- [52] M. Schwentenwein, P. Schneider, J. Homa, Lithography-based ceramic manufacturing: a novel technique for additive manufacturing of high-performance ceramics, 13th Int. Ceram. Congr. - Part B (2014), <https://doi.org/10.4028/www.scientific.net/ast.88.60>.
- [53] L. Conti, D. Bienenstein, M. Borlaf, T. Graule, Effects of the layer height and exposure energy on the lateral resolution of zirconia parts printed by lithography-based additive manufacturing, *Materials* 13 (2020), <https://doi.org/10.3390/ma13061317>.
- [54] M. Bergler, J. Korostoff, L. Torrecillas-Martinez, F.K. Mante, Ceramic printing-comparative study of the flexural strength of 3D-printed and milled zirconia, *Int. J. Prosthodont* 35 (2022) 777–783, <https://doi.org/10.11607/ijp.6749>.
- [55] D.A. Komissarenko, P.S. Sokolov, A.D. Evstigneeva, I.V. Slyusar, A.S. Nartov, P. A. Volkov, N.V. Lyskov, P.V. Evdokimov, V.I. Putlayev, A.E. Dosovitsky, DLP 3D printing of scandia-stabilized zirconia ceramics, *J. Eur. Ceram. Soc.* 41 (2021) 684–690, <https://doi.org/10.1016/j.jeurceramsoc.2020.09.010>.
- [56] R. He, W. Liu, Z. Wu, D. An, M. Huang, H. Wu, Q. Jiang, X. Ji, S. Wu, Z. Xie, Fabrication of complex-shaped zirconia ceramic parts via a DLP- stereolithography-based 3D printing method, *Ceram. Int.* (2018), <https://doi.org/10.1016/j.ceramint.2017.11.135>.
- [57] V. Stanic, N.N. Aldini, M. Fini, G. Giavaresi, R. Giardino, A. Krajewski, A. Ravaglioli, M. Mazzocchi, B. Dubini, M.G.P. Bossi, et al., Osteointegration of bioactive glass-coated zirconia in healthy bone: an in vivo evaluation, *Biomaterials* 23 (2002) 3833–3841.
- [58] M.W. Sa, B.N.B. Nguyen, R.A. Moriarty, T. Kamalidinov, J.P. Fisher, J.Y. Kim, Fabrication and evaluation of 3D printed BCP scaffolds reinforced with ZrO<sub>2</sub> for bone tissue applications, *Biotechnol. Bioeng.* (2018), <https://doi.org/10.1002/bit.26514>.